https://doi.org/10.5194/egusphere-2026-317
Preprint. Discussion started: 11 February 2026

Pre-Seismic Geomagnetic Fusion Anomaly Extraction Based on Spatially Weighted Non-Negative Tensor Factorization

Baiyi Yang, Kaiguang Zhu*, Ting Wang, Donghua Zhang, WenQi Chen, Yiqun Zhang, Pu Wang, Xingsu Li, and Yuqi Cheng

The College of Instrumentation and Electrical Engineering, Jilin University, Changchun 130000, China

Correspondence to: Kaiguang Zhu (zhukaiguang@jlu.edu.cn)

Abstract. Earthquake preparation processes are known to generate geomagnetic anomalies, Existing methods for extracting pre-seismic geomagnetic anomalies from multi-station observations are limited by the lack of physically meaningful constraints. Considering that electromagnetic signal propagation is related to epicentral distance, we incorporate spatial relationships between observation stations and potential seismic source regions into non-negative tensor factorization (NTF), and propose a Spatially Weighted Non-negative Tensor Factorization (SW-NTF) method to extract fused pre-seismic geomagnetic anomalies from multi-station data. SW-NTF was applied to daily 1 Hz Z-component geomagnetic data recorded at seven stations from 90 days before to 30 days after the 2021 Ms 7.4 Madoi earthquake. Compared with traditional NTF, SW-NTF captures a more pronounced accelerated growth in the pre-seismic geomagnetic anomalies. The extracted anomalies exhibit two phases of S-shaped accelerated growth (day −85 to −60 and day −40 to −17). Spatially, anomalous signals initially appear at stations farther from the epicenter and progressively migrate toward the epicentral region as the earthquake approaches. The potential influence of space weather activity is examined, suggesting that the detected anomalies are not dominated by external geomagnetic disturbances. Temporal comparisons show that the two-phase acceleration of geomagnetic anomalies precedes similar acceleration in cumulative Benioff strain. Observed variation patterns are also consistent with magnetic field changes in rock loading experiments, and the spatiotemporal correspondence with b-values indicates that the anomalies likely reflect stress evolution in the crust during earthquake preparation.

1 Introduction

Earthquakes, characterized by their sudden onset, high destructiveness, and formidability to predict, pose significant threats to human society. The journal Science has recognized earthquake prediction as one of the most challenging scientific problems worldwide. However, substantial studies have revealed that pre-seismic anomalies associated with the earthquake preparation process can manifest across the lithosphere, atmosphere, and ionosphere (Pulinets, 2004; Moore, 1964; Parrot et al., 1993; Ruzhin et al., 1998; Hayakawa, 2004). Monitoring these precursory anomalies and investigating their pre-seismic spatiotemporal patterns are thus of great importance for advancing earthquake prediction research. Among these precursors, seismo-electromagnetic anomalies are regarded as one of the most promising research avenues for achieving a breakthrough in earthquake prediction. Extensive studies have reported pre-seismic electromagnetic anomalies across a wide frequency spectrum, ranging from direct current (DC) to high frequency (HF), observed by both ground-based stations and satellite

https://doi.org/10.5194/egusphere-2026-317
Preprint. Discussion started: 11 February 2026

platforms (Gokhberg et al., 1982; Molchanov et al., 1995; Zlotnicki et al., 2006; Zhang et al., 2009; Huang, 2011; Zhima et al., 2012; Marchetti et al., 2020a; Huang et al., 2022; Yang et al., 2023; Marchetti et al., 2024).

Undoubtedly, ground-based stations are located closer to seismic sources than satellites, allowing pre-earthquake electromagnetic signals from underground to experience less attenuation before reaching the stations and enabling the detection of localized, small-scale anomalies. However, given the complexity of the Earth's electromagnetic environment, ground-based stations are susceptible not only to local interference, such as lightning, high-voltage direct current transmission lines, trams, or other anthropogenic disturbances, but also to global interference, including geomagnetic storms and solar activities. Consequently, studies relying on single-station data often struggle to accurately capture genuine pre-seismic electromagnetic anomalies. Some studies have attempted to perform pre-seismic electromagnetic anomaly extraction by integrating data from multiple ground stations and satellites (Xie et al., 2021; Chen et al., 2024). Hattori et al. applied principal component analysis (PCA) to geomagnetic observation data from multiple stations and extracted fused geomagnetic anomalies before the 2000 Izu Islands earthquake (Hattori et al., 2004). Yu et al. performed multichannel singular spectrum analysis (MSSA) on borehole strain data from multiple stations, removed periodic signals and noise from the dataset to extract seismic signals, and identified pre-seismic strain anomalies before several earthquakes through topological network analysis (Yu et al., 2020). Such approaches can extract common features from multi-station observation data, effectively reducing the randomness associated with individual observation platforms and enhancing the reliability of the results. In reality, geomagnetic anomalies are inherently spatiotemporal coupled events. The aforementioned methods mainly focus on temporal variations in the signals and lack the utilization of spatial information. Existing studies have shown that anomalous signals from the source region attenuate with increasing epicentral distance when propagating to stations at different distances (Xue et al., 2024; Han et al., 2014). Treating all stations at varying epicentral distances equally may therefore hinder the effective extraction of pre-seismic electromagnetic anomalies.

Based on the propagation characteristics of anomalous signals from seismic source regions (Wyss, 1991, 1997), we propose the spatially weighted non-negative tensor factorization for extracting fused geomagnetic anomalies prior to earthquakes. This method is designed to separate signal components with distinct spatial attenuation characteristics originating from the source region from the background field, thereby potentially enabling more direct correlation with physical processes at the hypocenter. Applying this novel methodology, we processed 1 Hz magnetic field data recorded by ground-based stations, provided by the China Earthquake Administration, to analyze anomalous geomagnetic changes preceding the Ms 7.4 Madoi earthquake in Qinghai, China. Section II provides a brief description of the Madoi earthquake and the data used. Section III introduces the Spatially Weighted Non-negative Tensor Factorization (SW-NTF) method. Section IV presents a comparison of the results from SW-NTF and traditional Non-negative Tensor Factorization (NTF), along with the spatiotemporal characteristics of the extracted pre-seismic geomagnetic anomalies. In Section 5, we discuss the influence of space weather on pre-seismic geomagnetic anomaly results and analyze the correspondence between laboratory rock experiments and pre-seismic anomalies. Finally, we compare the relationship between pre-seismic geomagnetic anomalies and seismic activity.

https://doi.org/10.5194/egusphere-2026-317
Preprint. Discussion started: 11 February 2026

2 Data and Seismic Event

2.1 Data

The geomagnetic field data used in this study were obtained from the China Earthquake Administration (https://data.earthquake.cn/index.html). All station instruments are GM-4 fluxgate magnetometers or their upgraded variants. The GM-4 fluxgate magnetometer is designed to measure relative variations in three components of the geomagnetic field: the horizontal intensity (H), vertical intensity (Z), and declination (D). For our analysis, we selected magnetic field data with a sampling rate of 1 Hz. This secondary data at 1 Hz sampling frequency fully retains electromagnetic characteristics in the ultra-low frequency (ULF) range (0.001–1 Hz), which holds particular value for seismo-electromagnetic studies (Han et al., 2011). Geomagnetic stations were initially selected with reference to the Dobrovolsky radius D ($D = 10^{0.43M}$ km, where M is the earthquake magnitude) (Dobrovolsky et al., 1979). Following the exclusion of stations subjected to severe interference (such as from geoelectrical resistivity anomalies, rail transit, or high-voltage direct current power lines) or those with significant data gaps, a total of seven geomagnetic stations were ultimately chosen. Table 1 presents the locations of these stations and their respective epicentral distances.

Table 1. Geomagnetic station information.

Station ID	Station Name	Longitude (°E)	Latitude (°N)	Epicentral Distance(km)
Sta_1	Dawu	100.25	34.48	175
Sta_2	Dulan	98.1	36.23	191
Sta_3	Delingha	97.39	37.38	321
Sta_4	Geermu	94.87	36.43	374
Sta_5	Xining	101.72	36.55	375
Sta_6	Tianshui	105.54	34.29	661
Sta_7	Yinchuan	106.28	38.5	830

2.2 Seismic Event

On May 21, 2021, an Ms 7.4 earthquake struck Madoi County in Qinghai Province, China. The epicenter was located at 34.59°N, 98.34°E, with a focal depth of 10 km (data sourced from the China Earthquake Administration, https://news.ceic.ac.cn/). This event stands as the largest earthquake to have occurred on the Chinese mainland since the 2008 Wenchuan earthquake. The Madoi earthquake occurred within the Bayan Har block, situated on the northeastern margin of the Tibetan Plateau, which is one of the most seismically active regions. Figure 1 shows the epicenter of the Madoi earthquake and the distribution of the stations.

https://doi.org/10.5194/egusphere-2026-317
Preprint. Discussion started: 11 February 2026

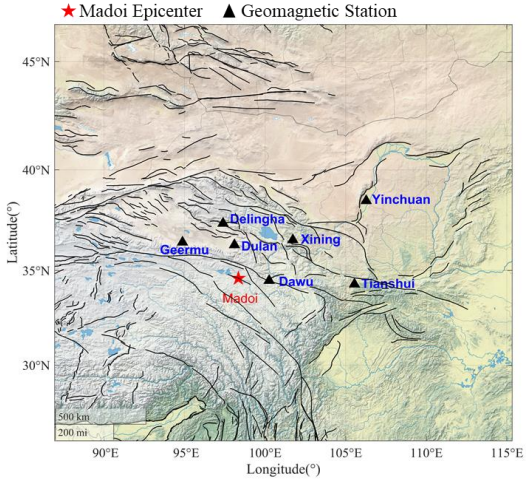

Figure 1: Epicenter of the Madoi earthquake and distribution of geomagnetic stations. The red star denotes the epicenter, black triangles represent geomagnetic stations, and black lines indicate fault lines.

3 Methodology

3.1 Spatially Weighted Non-negative Tensor Factorization

Non-negative Tensor Factorization (NTF) is a technique designed for multilinear dimensionality reduction and feature extraction of non-negative high-dimensional data. After decomposition, it can represent the primary local characteristics of the original data using a reduced amount of data (Hitchcock, 1928; Shashua and Levin, 2001). Applying NTF to decompose the third-order time-frequency spectral tensor enables accurate separation of seismic signals within the dataset. The introduction of coefficient components further allows for the representation of contributions from observation data across different stations to the anomalies. For instance, Fan et al. constructed a tensor from the magnetic field amplitude spectra of Swarm satellites A and C and employed NTF to extract magnetic field anomalies commonly recorded by both satellites, which may be associated with the 2015 Nepal earthquake (Fan et al., 2022). Building upon this, a similar technique was employed to extract fused anomalies in both the magnetic field and electron density recorded by Swarm satellites A and C before the 2021 Madoi earthquake (Fan et al., 2024), thereby demonstrating the robustness of NTF in the domain of pre-seismic fused anomaly extraction. Here, we construct a third-order tensor $X \in \mathbb{R}^{I\times J\times K}$ from the geomagnetic amplitude spectrum data recorded by multiple stations. Non-negative Tensor Factorization decomposes the original tensor into a sum of a finite number of rank-1 tensors, expressed as:

$$X \approx \sum_{r=1}^{R} a_r \circ b_r \circ c_r = [\![A, B, C]\!] \quad (1)$$

Where, R denotes the rank, indicating the number of features in the decomposition.$A \in \mathbb{R}^{I\times R}$ is the factor matrix of the first mode (Frequency), $B \in \mathbb{R}^{J\times R}$ is the factor matrix of the second mode (Time), and $C \in \mathbb{R}^{K\times R}$ is the factor matrix of the third mode (Space or Station Contribution). The symbol ∘ represents the vector outer product.

https://doi.org/10.5194/egusphere-2026-317
Preprint. Discussion started: 11 February 2026

During its decomposition process, NTF first randomly initializes the non-negative matrices A, B, and C. The objective function is then used to calculate the discrepancy between the original tensor and the decomposition result. Subsequently, iterative optimization is applied to minimize the objective function and obtain the factor matrices (Hansen et al., 2015). The objective function of traditional Non-negative Tensor Factorization can be expressed as:

$$\min_{A,B,C\geq 0} \left\| X - \sum_{r=1}^{R} a_r \circ b_r \circ c_r \right\|_F^2 \tag{2}$$

Where, $A = [a_1, \cdots, a_R] \in \mathbb{R}^{I\times R}$,$B = [b_1, \cdots, b_R] \in \mathbb{R}^{J\times R}$ and $C = [c_1, \cdots, c_R] \in \mathbb{R}^{K\times R}$.

The iterative optimization update rules for NTF follow the Alternating Least Squares (ALS) framework, are derived via gradient descent, and ensure non-negativity (Hansen et al., 2015). Specifically, the update rules are expressed as:

$$A \leftarrow A \odot \frac{X_{(1)}(C \odot B)}{A[(C^T C) \odot (B^T B)]} \tag{3}$$

$$B \leftarrow B \odot \frac{X_{(2)}(C \odot A)}{A[(C^T C) \odot (A^T A)]} \tag{4}$$

$$C \leftarrow C \odot \frac{X_{(3)}(B \odot A)}{A[(B^T B) \odot (A^T A)]} \tag{5}$$

Where, $\odot$ denotes the element-wise multiplication (Hadamard product), and the division is performed element-wise.

After each iteration, the Karush-Kuhn-Tucker (KKT) conditions are used to determine whether the results have converged (Fan et al., 2022; Chi and Kolda, 2012). The iterative process terminates when either the KKT conditions are satisfied or the maximum number of iterations is reached, yielding the final factor matrices.

In traditional NTF, the decomposition process relies solely on the statistical properties of the data, treating records from all stations equally. However, during decomposition, traditional NTF relies solely on the statistical properties of the data and treats records from all stations equally. This means that global interference signals—such as geomagnetic storms and traveling ionospheric disturbances (TIDs)—which exhibit broad spatial coverage and consistency, are likely to manifest similarly across all stations (Yao et al., 2016; Habarulema et al., 2018). As a result, these interfering signals can be captured within one or a few components, making them difficult to distinguish from seismic anomalies. Furthermore, if certain stations are severely contaminated by noise, their anomalous values may disproportionately influence the global loss function.

Based on the widely accepted observation that seismo-electromagnetic anomalies attenuate with increasing epicentral distance (Wyss, 1997; Hattori, 2004; Schekotov et al., 2007; Han et al., 2014; Xue et al., 2024; Feng et al., 2025), we introduce spatial weighting into the NTF of geomagnetic data. This approach incorporates physical prior knowledge—specifically, the spatial relationship between stations and potential seismic source areas—as a constraint into the decomposition process, which originally relied solely on data statistics. Consequently, the extracted components are not only distinguishable in the time-frequency domain but also more physically meaningful in the spatial domain, thereby enabling more precise isolation of genuine anomaly signals associated with earthquake preparation.

https://doi.org/10.5194/egusphere-2026-317
Preprint. Discussion started: 11 February 2026

The proposed method is named Spatially Weighted Non-negative Tensor Factorization (SW-NTF). It is designed to place greater emphasis on stations near the epicenter, thereby guiding the decomposition process toward a physically more plausible solution space. Specifically, an epicentral distance weight vector for geomagnetic stations is constructed: $\omega = [w_1, w_2, \cdots w_K]^T \in \mathbb{R}^K$, where w_K represents the weight of the k-th station. The weight assignment follows an inverse relationship with the epicentral distance, meaning a smaller distance corresponds to a larger weight. The modified objective function is then formulated as:

$$\min_{A,B,C\geq 0} \left\| X - \sum_{r=1}^{R} a_r \circ b_r \circ c_r \right\|_F^2 + \lambda \sum_{r=1}^{R} \|c_r - \omega\|_2^2 \tag{6}$$

In the equation, λ denotes the regularization coefficient, while the remaining parameters are consistent with traditional NTF. It is important to note that the regularization term is applied solely to the space (Station Contribution) factor matrix C. Therefore, in SW-NTF, the update rules for the frequency factor matrix A and the time factor matrix B remain consistent with traditional NTF. However, due to the incorporation of the regularization term for the matrix C, its multiplicative update rule is modified: the denominator includes the positive part of the regularization term's derivative, while the numerator incorporates the negative part. The update rule for the matrix C is given as follows:

$$C \leftarrow C \odot \frac{X_{(3)}(B \odot A) + \lambda\omega}{A[(B^T B) \odot (A^T A)] + \lambda C} \tag{7}$$

The complete procedure of the Spatially Weighted NTF algorithm is summarized as follows:

1) Initialization: Randomly initialize the non-negative matrices A, B, and C.

2) Iteration: (until convergence or the maximum number of iterations is reached):

a. Update the frequency factor matrix A (with other factors fixed).

b. Update the time factor matrix B (with other factors fixed).

c. Update the space factor matrix C (with other factors fixed and incorporating the spatial regularization).

d. Calculate the reconstruction error.

3) Normalization: Normalize the column vectors of each factor matrix while preserving their product.

3.2 Data Processing

In this section, we construct a third-order tensor using 1 Hz observation data of the Z-component from seven geomagnetic stations and perform tensor decomposition to extract pre-seismic electromagnetic anomaly signals. Generally, geomagnetic observation data primarily consist of the following components: global magnetic disturbances, local magnetic disturbances (e.g., sources such as anthropogenic noise and meteorological activities), and magnetic signals originating from subsurface activities (Hattori et al., 2013b). To minimize the influence of anthropogenic noise, this study selects and processes Z-component data from the local midnight period (00:00–04:00 LT).

https://doi.org/10.5194/egusphere-2026-317
Preprint. Discussion started: 11 February 2026

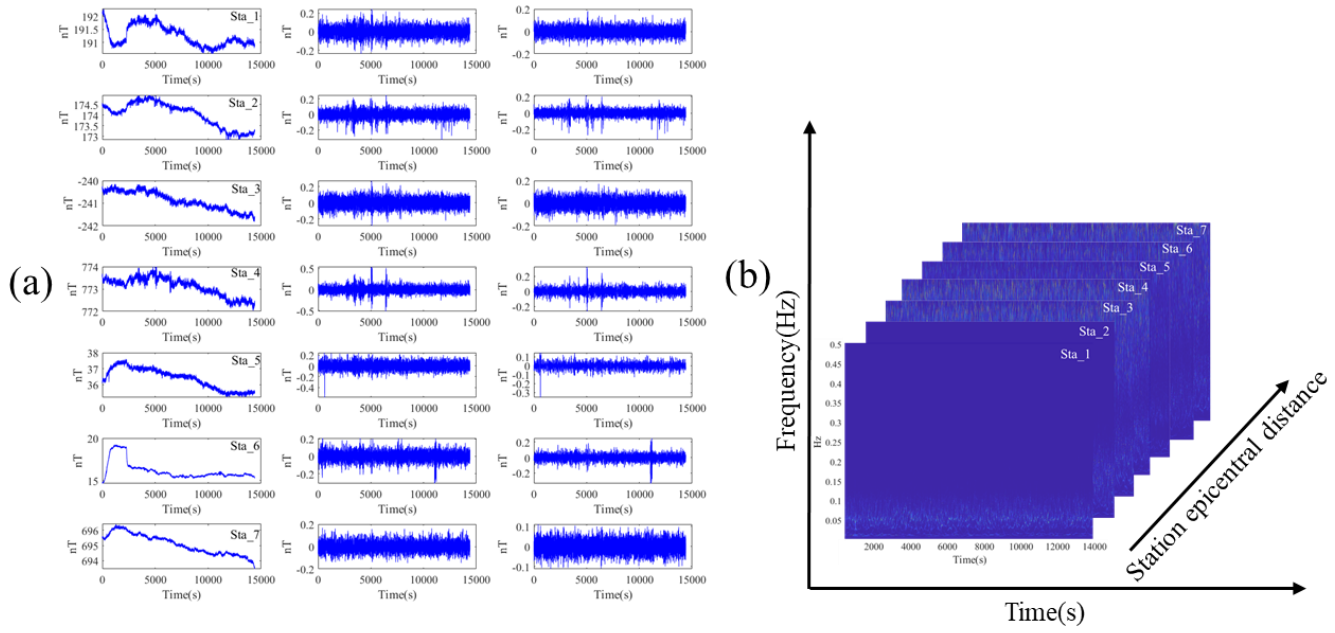

Figure 2: Data preprocessing. In (a), the first column displays the original data from the seven stations, the second column presents the detrended signals for each station, and the third column shows the reconstructed signals after high-frequency noise removal using MEMD. Subplot (b) illustrates the third-order tensor constructed from the time-frequency amplitude spectra of the seven stations.

Figure 2 illustrates the data preprocessing workflow using the data from May 2, 2021, as an example. Column 1 of Figure 2(a) displays the original waveforms of geomagnetic data from seven stations. The data preprocessing pipeline consists of three key stages. First, to eliminate the diurnal variation trend in the geomagnetic data, we employed a 6-level Discrete Wavelet Transform (DWT) with the db5 wavelet basis (Han et al., 2011; Hattori et al., 2013b). The low-frequency background was removed by discarding the approximation coefficients from the final decomposition level, with the result after low-frequency removal shown in the second column of Figure 2(a). Subsequently, to suppress high-frequency noise, multivariate empirical mode decomposition (MEMD) was employed to decompose the data from the seven stations. For each station, the kurtosis and energy entropy of each intrinsic mode function (IMF) were calculated. IMFs with kurtosis > 3 and energy entropy < 0.3 were selected and reconstructed to obtain the denoised signals (Rehman and Mandic, 2010; Liu et al., 2018; Li et al., 2020), as presented in the third column of Figure 2(a). Finally, the Wavelet Synchro-squeezed Transform (WSST) was utilized to obtain the time-frequency amplitude spectrum of the reconstructed data from each station. A third-order non-negative tensor was subsequently constructed using the daily time-frequency amplitude spectra from all seven stations, with its three dimensions representing frequency, time, and station contribution, as illustrated in Figure 2(b).

We applied the SW-NTF to decompose the daily tensor constructed from the seven stations. The parameters were set as follows: regularization coefficient λ =0.1, maximum iterations=200, and convergence tolerance under KKT conditions=0.00001. Based on the actual situation that geomagnetic observation data may contain seismic signals, local

https://doi.org/10.5194/egusphere-2026-317
Preprint. Discussion started: 11 February 2026

magnetic disturbances, and global magnetic disturbances, the number of decomposition features $R = 3$. The decomposition yields three non-negative factor matrices: $A = [a_1, a_2, a_3]$ (frequency), $B = [b_1, b_2, b_3]$ (time), and $C = [c_1, c_2, c_3]$ (station contribution). The three vectors in matrix A represent the spectral characteristics of each component in the geomagnetic data, the three vectors in B depict their temporal variations, and the three vectors in C indicate the contribution of each station to these components.

Due to the inherent unordered nature of NTF decomposition results, we need to identify components potentially associated with seismic activity. In previous studies, one of the most frequently reported frequency ranges for seismo-electromagnetic phenomena is 0.01–0.05 Hz (Fraser-Smith et al., 1990; Hayakawa et al., 1996; Hattori et al., 2013b; Hattori et al., 2013a; Hayakawa et al., 2023; Han et al., 2014; Hattori, 2004). We defined a frequency ratio coefficient η_r (calculated as the ratio of the energy within the 0.01–0.05 Hz range to the total energy of each vector in the frequency matrix A). The components were then sorted in descending order of this coefficient, resulting in the sequences $a_{s1}(b_{s1}, c_{s1}), a_{s2}(b_{s2}, c_{s2})$, and $a_{s3}(b_{s3}, c_{s3})$. The component $a_{s1}(b_{s1}, c_{s1})$ was selected as the seismically relevant component, and its corresponding temporal feature vector b_{s1} was subsequently used to extract potential pre-seismic anomalies. Figure 3 compares the decomposition results of traditional NTF and SW-NTF for May 2nd, one day before the earthquake.

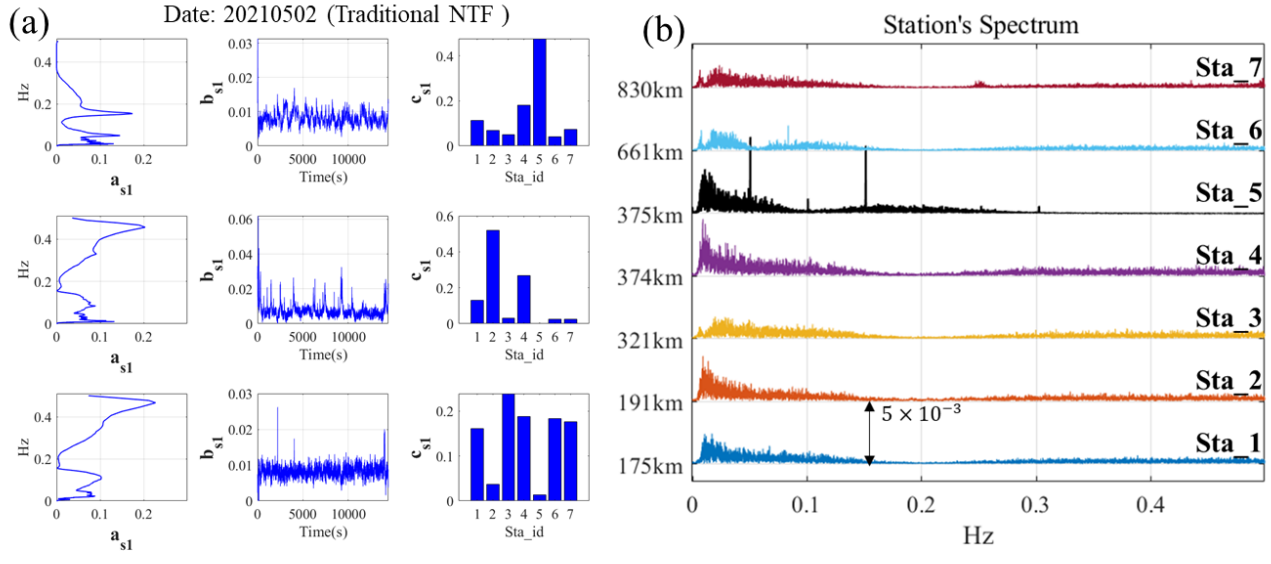

Figure 3: Decomposition results for traditional NTF on May 2. (a) Traditional NTF decomposition results, the first column represents the frequency vector a_s, the second column shows the time vector b_s, and the third column indicates the station contribution vector c_s. (b) Spectra from seven stations on May 2.

In traditional NTF, the lack of constraints during the decomposition process often leads to unstable results due to random noise in the data or instrument failures at individual stations. For example, in Figure 3(a), the energy of the component considered seismically relevant, a_{s1}, is predominantly concentrated around 0.05 Hz and 0.15 Hz. Further examination of its corresponding station contribution c_{s1} reveals that Sta_5, located farther from the epicenter, dominates this component. As observed in Figure 3(b), the spectrum of Sta_5 exhibits prominent energy peaks at 0.05 Hz and 0.15 Hz, which likely

https://doi.org/10.5194/egusphere-2026-317
Preprint. Discussion started: 11 February 2026

represent far-field interference signals. Clearly, such interference affects the decomposition outcome of conventional NTF. Moreover, in the traditional NTF results, the spectral features a_{s2} and a_{s3} both show primary energy around 0.45 Hz. The fact that structures with similar spectral characteristics are separated into two distinct components indicates that the conventional method lacks adequate discriminative ability in component separation.

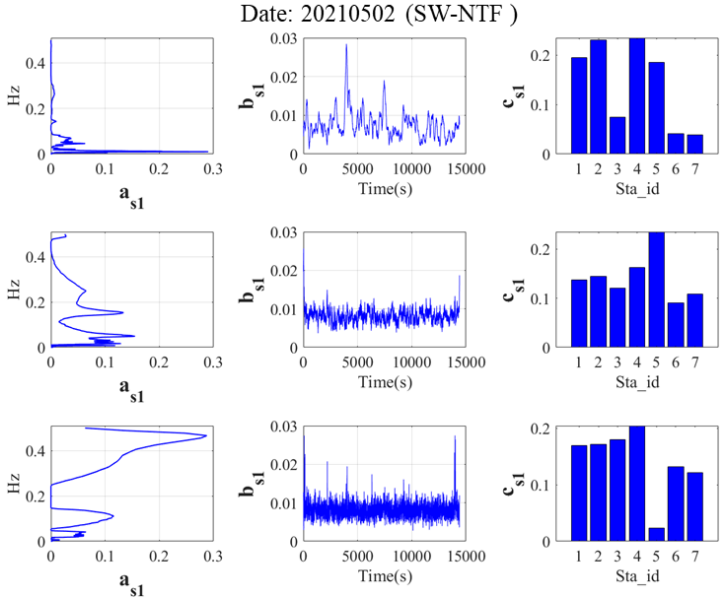

Figure 4: Decomposition results for SW-NTF on May 2

In contrast, the application of SW-NTF yields smore satisfactory results. The spatial weighting strategy inherently suppresses the contribution of such noise signals in key components, as the algorithm is designed to identify signal patterns that are prominent in high-weight regions (e.g., near the epicenter) yet faint in low-weight regions, precisely the characteristic of localized seismic anomalies. As shown in Figure 4, in the frequency vector, the energy of a_{s1} is primarily concentrated around 0.01 Hz, indicating that potentially earthquake-related anomalies have been effectively extracted. Meanwhile, in the station contribution vector c_{s1}, several stations closer to the epicenter exhibit similar contribution levels, reflecting spatial consistency. Furthermore, the energy of a_{s2} is mainly distributed around 0.05 Hz and 0.15 Hz, while the frequency content of the third component a_{s3}, is predominantly concentrated near 0.45 Hz. These results demonstrate the superior performance of SW-NTF in signal separation.

4 Result

4.1 Temporal Cumulative Results of Geomagnetic Anomalies

We analyzed 120 days spanning from 90 days before to 30 days after the Madoi earthquake. Daily geomagnetic data were structured into tensors and decomposed using SW-NTF, with anomalies subsequently extracted from the temporal feature

https://doi.org/10.5194/egusphere-2026-317
Preprint. Discussion started: 11 February 2026

matrix B. To enhance detection accuracy, we adopted established criteria for identifying seismo-electromagnetic anomalies, requiring simultaneous satisfaction of two conditions: the anomaly amplitude must exceed $k * \sigma$ (where k=5) and its duration must fall within the range $t\_min < t < t\_max$ (with t_{min}=60s and t_{max}=300s) (Li and Parrot, 2012; Li and Parrot, 2013; Zhang et al., 2023). Figure 4 presents a comparative analysis of the cumulative anomalies derived from the seismically relevant component (b_{s1}) against those from the other two components (b_{s2} and b_{s3}) during the observational period.

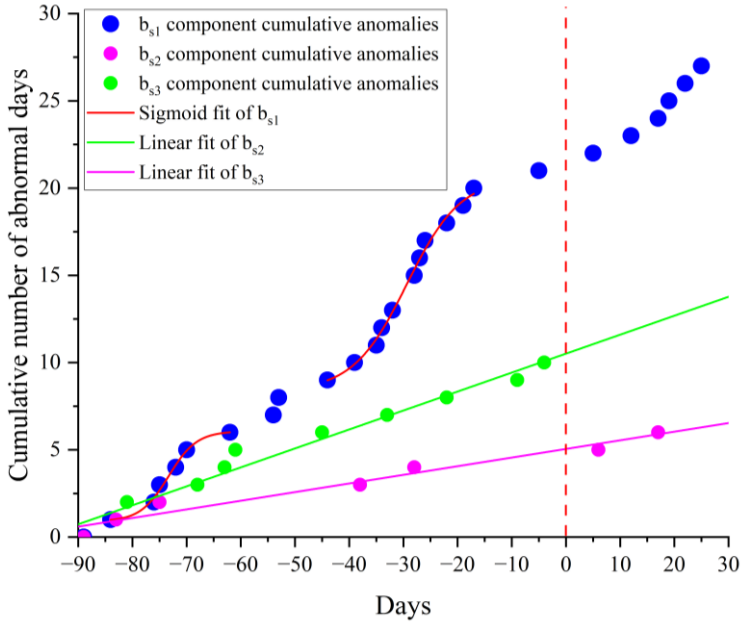

Figure 5: Cumulative anomaly results of the three b_s components from SW-NTF. The red S-shaped curve represents the sigmoidal fit of the non-linear acceleration, while the pink and green solid lines show the linear fitting results for the b_{s2} and b_{s3} components, respectively. The red dashed line indicates the occurrence time of the mainshock.

Figure 5 reveals two distinct phases of accelerated growth in the earthquake-related b_{s1} component before the mainshock. During these periods, geomagnetic anomalies occurred frequently. This observation aligns with numerous previous studies reporting that pre-seismic electromagnetic anomalies often exhibit discontinuous, burst-like, and clustered occurrence patterns (Marchetti et al., 2020a; Marchetti et al., 2020b; De Santis et al., 2017; Marchetti and Akhoondzadeh, 2018; De Santis et al., 2019b; Zhu et al., 2021). We characterized these two phases of anomalous acceleration using a Sigmoid function, expressed as:

$$S_{sigmoid}(t) = A_2 + \frac{(A_1 - A_2)}{\left(1 + e^{\frac{(x-x_0)}{d_x}}\right)} \tag{8}$$

Where A_1, A_2, and d_x represent the lower asymptote, upper asymptote, and time constant, respectively, while x_0 denotes the inflection point—the center of the function where the growth rate reaches its maximum.

https://doi.org/10.5194/egusphere-2026-317
Preprint. Discussion started: 11 February 2026

The Sigmoid fitting demonstrates high sensitivity to deviations from linear growth patterns. In contrast, the occurrence frequency of anomalies in stochastic systems tends to be stable, resulting in a linear accumulation over time (De Santis et al., 2015; De Santis et al., 2017). In other words, an S-shaped growth pattern suggests a potential correlation with seismic activity, whereas a linear growth pattern typically indicates anomalies unrelated to earthquakes.

The first sigmoidal phase was fitted from day -85 to -60, with an inflection point x_0 at -73.3 days and a coefficient of determination R^2 of approximately 0.98. The second phase was fitted from day -40 to -17, with x_0=-29.3 days and $R^2 \approx 0.99$. These high R^2 values indicate excellent fitting performance, confirming that the cumulative anomalies during both nonlinear acceleration phases follow a sigmoidal growth pattern. Conversely, the growth trends of components b_{s2} and b_{s3} align with linear models, supporting their classification as seismically unrelated components.

Another noteworthy observation is that from approximately 20 days before the earthquake until its occurrence, the cumulative results of the b_{s1} component show only very few geomagnetic anomalies. Previous studies have indicated that a period of quiescence often precedes major earthquakes worldwide (Wyss et al., 1997; Gentili et al., 2019). Similar observations have been demonstrated in laboratory experiments, where a brief cessation of acoustic emission signals was observed prior to rock failure. This phenomenon has been attributed to the concept of dilatancy hardening in the region surrounding an impending earthquake (Scholz, 1988). These findings suggest that the temporal variation of pre-seismic anomalies may be linked to the preparation process of the Madoi earthquake.

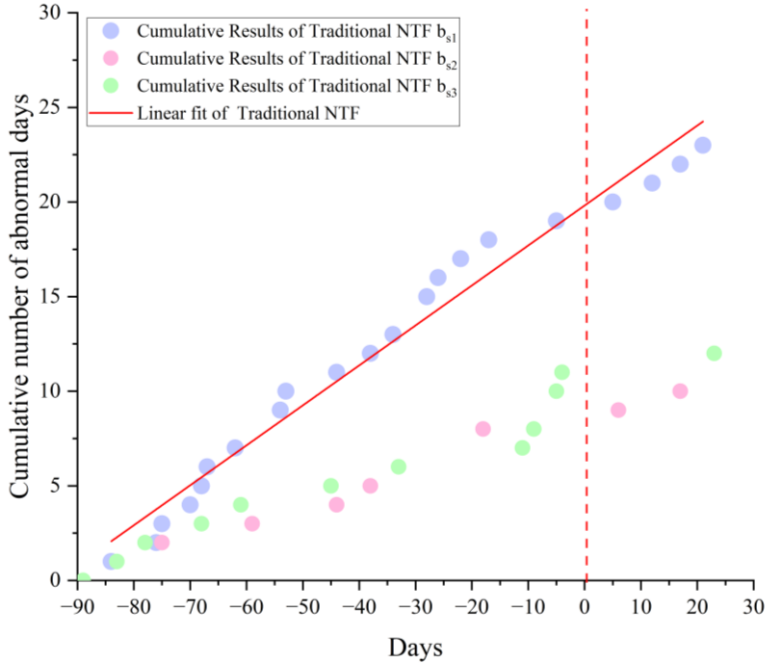

Figure 6: Temporal cumulative anomaly results from traditional NTF. The red solid line shows the linear fit to the cumulative anomalies obtained by traditional NTF, and the red dashed line marks the occurrence time of the mainshock.

https://doi.org/10.5194/egusphere-2026-317
Preprint. Discussion started: 11 February 2026

For comparison, we accumulated the anomalies extracted by traditional NTF to obtain Figure 6. Specifically, around 70 days before the earthquake, a phase of acceleration is observed, followed by another between days -30 and -20. However, compared to SW-NTF, these acceleration phases are less pronounced and progress more gradually. During the remaining periods, the cumulative trend remains predominantly linear. Overall, the cumulative anomalies from traditional NTF exhibit a linear growth pattern, with a coefficient of determination (R^2) of approximately 0.97 for the linear fit. This indicates that our proposed SW-NTF appears to be more effective in extracting pre-seismic electromagnetic anomalies.

4.2 Spatial Characteristics of Geomagnetic Anomalies

Beyond analyzing the temporal characteristics of geomagnetic anomalies, we further investigated their spatial evolution before the earthquake. The station contribution matrix in SW-NTF enables us to reflect the contribution of each station's observational data to the daily fused geomagnetic anomalies. Based on the station contribution matrix C obtained from the daily decomposition results, we can identify the stations that make primary contributions. This allows us to illustrate the spatial evolution of pre-seismic anomalies and investigate the earthquake preparation process, as shown in Figure 7.

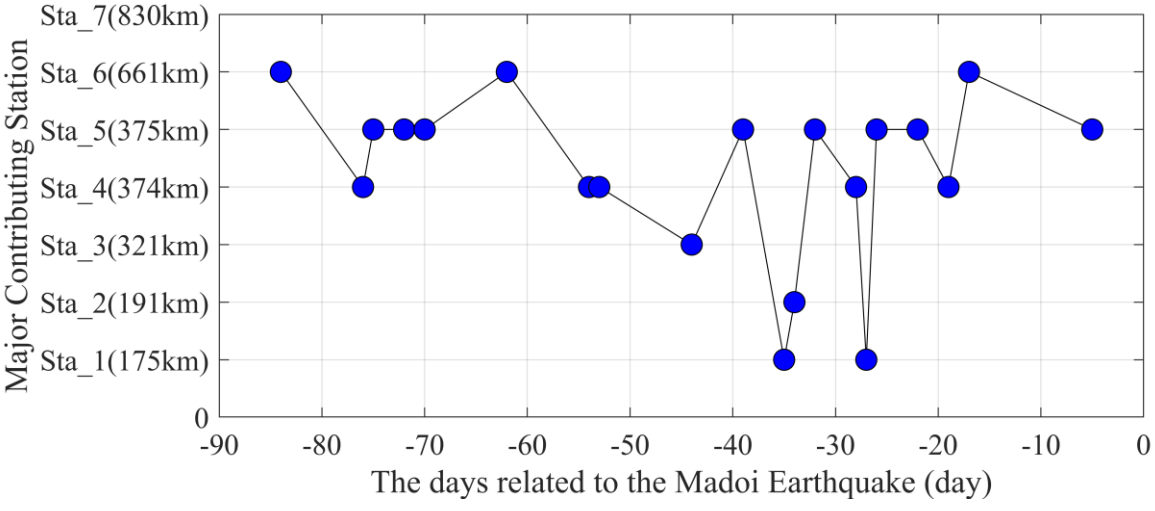

Figure 7: Temporal Variation of Primary Contributing Stations in the geomagnetic anomalies before the Madoi earthquake.

From approximately day -90 to day -27, a clear spatial migration pattern is observed: the station with the maximum contribution coefficient gradually shifts from those farther from the epicenter to those closer to it, with all maximum contribution coefficients ranging between 0.4 and 0.7. This indicates that during this phase, the spatial location of the dominant station in the fused anomalies progressively migrated toward the epicenter. However, beginning about one month before the earthquake, the stations exhibiting the maximum contribution were exclusively located beyond approximately 350 km from the epicenter, with no stations near the epicenter showing dominant contributions. The distinct difference in spatial evolution between these two phases may reflect changes in subsurface stress. Moreover, in existing studies on the pre-seismic period of the Madoi earthquake, similar temporal patterns of quiescence were observed in thermal anomaly

https://doi.org/10.5194/egusphere-2026-317
Preprint. Discussion started: 11 February 2026

parameters, such as the Microwave Brightness Temperature (MBT) and Outgoing Longwave Radiation (OLR), within the epicentral area (Jing et al., 2022; Liu et al., 2023; Yang et al., 2025). Ma et al. suggest that in heterogeneous media, faults contain both weak and strong segments. During the initial stage of stress loading, micro-fracturing and slip tend to occur in the relatively weak zones—often at the edges of the seismogenic area—releasing stress. As stress continues to accumulate and concentrate on the strong, locked segments, the fault enters a locked phase, making a large earthquake inevitable (Ma and Guo, 2014). This model is largely consistent with our observed spatiotemporal changes in pre-seismic anomalies: geomagnetic anomalies first migrate toward the epicenter, followed by a period of quiescence in the epicentral area, after which the mainshock occurs.

5 Discussion

5.1 Analysis of Space Weather Impacts

Since geomagnetic observations are susceptible to interference from magnetic storms and solar activity, we investigated the space weather conditions during the study period. The Dst and ap indices were used to assess geomagnetic activity levels (data sourced from the World Data Center for Geomagnetism, Kyoto, https://wdc.kugi.kyoto-u.ac.jp/). Based on the classification criteria for Dst proposed and the standard classification for the ap index by Loewe and Prölss, and relevant experience in earthquake studies (Loewe and Prölss, 1997; Yao et al., 2016; Ouyang et al., 2020), we categorized the geomagnetic activity intensity into three levels, from weak to strong. The geomagnetic activity levels corresponding to the periods with observed anomalies are summarized in Table II.

Table 1. Number of anomalies under different geomagnetic conditions

Parameter	Level	Number of anomalies
Dst	$\|Dst\| \leq 30$ (nT)	25
	$30 < \|Dst\| \leq 50$ (nT)	2
	$\|Dst\| > 50$ (nT)	0
ap	$ap \leq 32$	27
	$32 < ap \leq 48$	0
	$ap > 48$	0

The results indicate that the observed geomagnetic anomalies occurred almost exclusively during periods of low geomagnetic activity, with only two exceptions under moderate activity levels. This demonstrates that the anomalies are independent of strong geomagnetic disturbances, implying that the seismically relevant anomalies extracted by SW-NTF are not caused by intense space weather events. Therefore, it can be concluded that SW-NTF is capable of extracting geomagnetic anomalies potentially related to seismic processes.

https://doi.org/10.5194/egusphere-2026-317
Preprint. Discussion started: 11 February 2026

5.2 Temporal Variations in the Amplitude of Geomagnetic Anomalies and Potential Mechanisms

In addition to analyzing the spatiotemporal evolution characteristics of pre-seismic anomalies, we also examined variations in the amplitude of the fused anomaly before the earthquake. The anomaly amplitude was obtained by reconstructing the time-domain signal from the seismically relevant component b_{s1} (a_{s1} and c_{s2}), with the results presented in Figure 8.

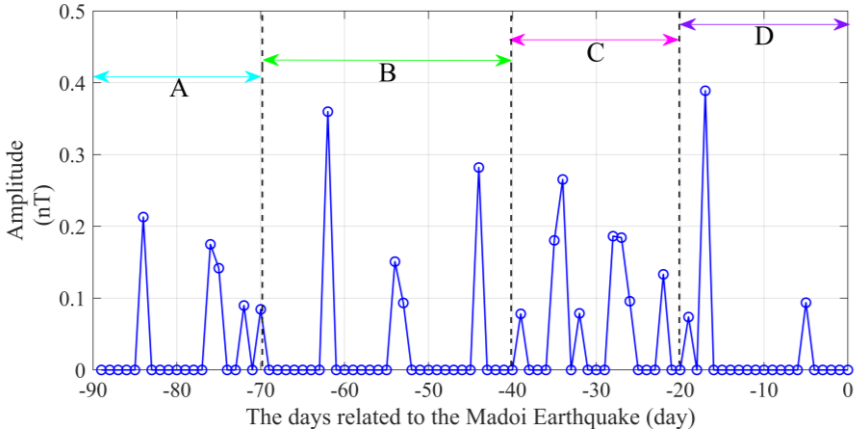

Figure 8: Temporal variation in the amplitude of geomagnetic fusion anomalies before the Madoi Earthquake. The blue curve represents amplitude variation.

Overall, Overall, the magnitude of pre-earthquake geomagnetic anomalies ranged between 0.1-0.4 nT, which corresponds to the widely reported range of pre-earthquake magnetic field anomaly variations (Marchetti and Akhoondzadeh, 2018; Kelley et al., 2017; Utada et al., 2011). The amplitude of the pre-seismic fused geomagnetic anomaly exhibits an increasing trend. Multiple peaks occur before the earthquake, with their magnitudes rising progressively. Approximately 18 days before the event, the amplitude of the fused anomaly reaches its maximum. This phenomenon may indicate that the source region underwent a nonlinear, intermittent process of stress accumulation and release during the impending seismic stage. We suggest that this periodic anomaly pattern, characterized by accelerating amplitude growth, could represent an electromagnetic manifestation of the fault system transitioning into a critical state before instability. He et al. (2023) experimentally analyzed the magnetic field characteristics generated by rocks at different loading stages, and the pre-seismic fused magnetic anomalies we extracted exhibit similar variations. During the initial compaction phase A (-90 to -70 days in Figure 8), the magnetic induction intensity fluctuates and increases. In this stage, the magnetic field is mainly produced by current variations caused by inter-granular friction and the slip-rubbing along primary pores and fractures within the rock. In the elastic deformation phase B (-70 to -40 days), the magnetic induction intensity shows a steadily increasing trend, with the magnetic field primarily generated by the piezoelectric polarization current effect. During the crack propagation phase C (-40 to-20 days), the initiation and growth of internal cracks, along with associated frictional slip, produce varying currents, leading to a rapid increase in magnetic induction intensity. Here, the magnetic field results not only from a minor contribution of the piezoelectric effect, but is mainly attributed to frictional current effects and crack-extension current

https://doi.org/10.5194/egusphere-2026-317
Preprint. Discussion started: 11 February 2026

effects. The anomaly amplitude at this stage approaches 0.2 nT, this experimental result aligns with the theoretical value obtained by Venegas-Aravena et al. (2019), indicating that when fractures form in the semi-brittle-ductile zone (depth 10–20 km), the magnetic field increases by approximately 0.2 nT. In the failure phase D (from about -20 days until the earthquake occurs), a large number of micro-cracks propagate, intersect, and coalesce rapidly within the rock, eventually connecting to form visible macroscopic cracks. The magnetic induction intensity rises sharply during this stage; the greater the number of cracks and the faster their propagation, the larger the induced current. It should be emphasized that although the time scale of our observational period (90 days) cannot be directly matched with the duration of the rock experiment (approximately 200 s), the trend of magnetic field variations observed in the laboratory experiment can still be used to examine the plausibility of the pre-seismic magnetic anomalies identified in our study.

5.3 Comparative Analysis with Cumulative Benioff strain

Pre-seismic electromagnetic anomalies originate from subsurface processes. To investigate the correlation between the extracted anomalies and seismic activity, we compare the temporal cumulative characteristics of the pre-seismic electromagnetic anomalies with those of lithospheric seismicity. The earthquake catalog is sourced from the China Earthquake Administration (https://news.ceic.ac.cn/), covering an area within ±2° from the epicenter, which corresponds to approximately a 400 km rupture zone for the Madoi earthquake (Li et al., 2025). The cumulative Benioff strain is used to describe the incremental strain rebound occurring on faults within the study area (Benioff, 1949; De Santis et al., 2015). The formula for calculating the cumulative Benioff strain S is as follows:

$$S(t) = \sum_{i=1}^{N(t)} \sqrt{10^{4.8+1.5M_i}} \tag{9}$$

where M_i is the magnitude of the ith earthquake and $N(t)$ is the total number of earthquakes until time t.

Before large earthquakes, an increase in small earthquake sequences is often observed (Brace and Byerlee, 1966). However, due to the limited detection capability of seismic networks, some smaller-magnitude events may go unrecorded. Therefore, it is necessary to determine the completeness magnitude M_c, which represents the minimum magnitude that can be fully detected within the study region. We estimated M_c using the maximum curvature method (Wiemer and Wyss, 2000), yielding a value of 0.71. Subsequently, shallow-focus earthquakes with focal depths less than 50 km were selected from the catalog to calculate the cumulative Benioff strain S. The temporal variations of the cumulative geomagnetic anomalies and the cumulative Benioff strain in the lithosphere are shown in Figure 9.

https://doi.org/10.5194/egusphere-2026-317
Preprint. Discussion started: 11 February 2026

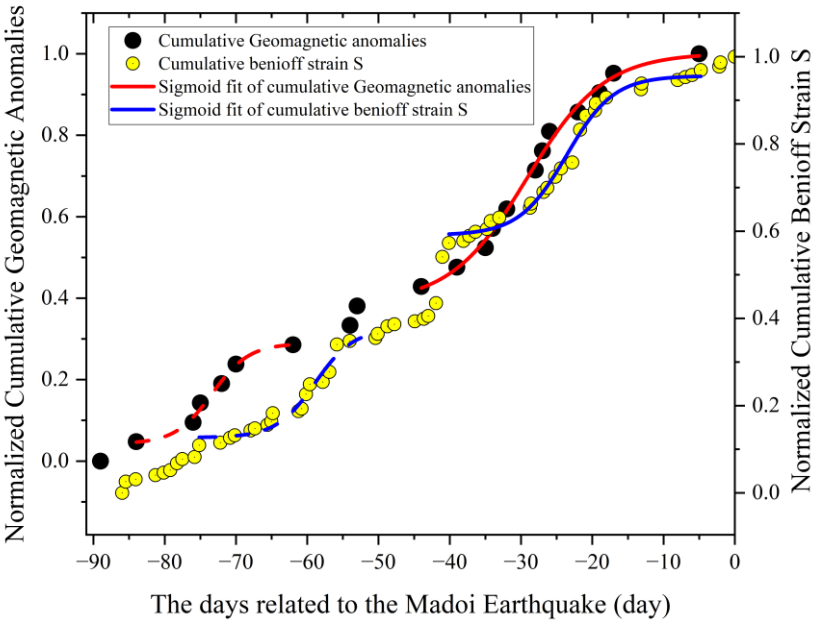

Figure 9: Comparison between cumulative geomagnetic anomalies and cumulative Benioff strain. Black dots represent cumulative geomagnetic anomalies, yellow dots denote cumulative Benioff strain, red and blue curves show the sigmoidal fits for the geomagnetic anomalies and cumulative Benioff strain, respectively. Dashed lines indicate the first acceleration phase, while solid lines represent the second acceleration phase.

In Figure 9, the cumulative Benioff strain, represented by the yellow dots, exhibits two distinct phases of accelerated growth. Similarly, we applied the sigmoid function introduced in Section III to fit these phases. The first phase, spanning approximately from day -75 to -50 (depicted by the blue dashed sigmoidal curve in the figure), has a coefficient of determination (R^2) of about 0.96. The second phase, from approximately day -40 to -5 (represented by the blue solid sigmoidal curve), shows an R^2 of approximately 0.99. The consistency of these two accelerated growth phases across both geophysical datasets suggests the existence of two critical stages before the mainshock. This observation aligns with the findings of Ma and Guo, indicating the possible occurrence of a meta-instability stage and two unstable fault deformation stages before the seismic event (Ma and Guo, 2014).

It is noteworthy, however, that in both phases, the acceleration of geomagnetic anomalies preceded that of the cumulative Benioff strain by approximately 5 to 15 days. This temporal offset can be attributed to the fact that Benioff strain primarily reflects macroscopic-scale rock rupture and slip. Significant acceleration in strain rate occurs only when a substantial number of microcracks have formed, propagated, and interconnected. In contrast, systematic changes in the microscopic physical properties (such as magnetic and electrical characteristics) of rocks in the source region already take place before crustal stress accumulates sufficiently to generate a notable macroscopic rupture (manifested as accelerated Benioff strain).

In Scholz's dilatancy-diffusion model, it is proposed that dilatancy initiates when the stress reaches approximately half the rock's fracture strength, a stage characterized by the nucleation and growth of microcracks (Scholz et al., 1973). Molchanov and Hayakawa suggested that charge separation occurs on the opposing surfaces of newly formed microcracks, generating

https://doi.org/10.5194/egusphere-2026-317
Preprint. Discussion started: 11 February 2026

transient currents and emitting electromagnetic waves (Molchanov and Hayakawa, 1995). The generation of such microcracks alters the pore structure and connectivity of the rock, thereby affecting resistivity and subsequently leading to magnetic anomalies (Xue et al., 2014). In summary, geomagnetic anomalies capture signals indicating that "the rock has begun to be damaged," whereas the acceleration of Benioff strain reflects the process whereby "the damage has accumulated to a certain extent and begins to propagate."

5.4 Spatiotemporal Correlation Between Geomagnetic Anomalies and b-value

Existing studies have demonstrated that the b-value reflects the magnitude-frequency distribution of earthquakes within a specific region and serves as an indicator of the subsurface stress state. An observed decrease in b-value before seismic events is widely regarded as a manifestation of increasing stress accumulation (Scholz, 1968; Schorlemmer et al., 2005). The b-value is derived from the Gutenberg-Richter law:$\log N = a - bM$, where M represents the earthquake magnitude, and N denotes the number of earthquakes with magnitudes greater than M. This relationship is commonly referred to as the G-R relation (Gutenberg and Richter, 1944). An increase in the b-value indicates a higher probability of occurrence for smaller seismic events. We calculated the b-value using the maximum likelihood estimation method (K., 1965):

$$b = \frac{1}{\ln(10)\,(\bar{M} - M_C)} \tag{10}$$

Where $\bar{M}$ is the average magnitude of all earthquakes in the target catalog sample with magnitudes greater than M_C, and M_C represents the minimum completeness magnitude. The confidence interval for the b-value can be estimated using Equation:

$$\sigma_b = \frac{b}{\sqrt{N}} \tag{11}$$

Where N represents the total number of events in the given sample.

Finally, we calculated the b-values for the period spanning 90 days before the earthquake within a $\pm 7°$ range around the epicenter, using a 3-day moving window with a 1-day step and setting a minimum of 20 seismic events. Figure 10 illustrates the relationship between the cumulative geomagnetic anomalies and the temporal characteristics of the pre-seismic b-values. Figure 10(a) shows that the inflection points x_0 of the two S-shaped growth phases for the geomagnetic anomalies are located at -73.3 days and -29.3 days, respectively. The inflection point in a sigmoidal fit is generally considered to correspond to a critical point in a non-random system: as this point is approached, anomalies accelerate, and the rate of increase decelerates thereafter (De Santis et al., 2019a). In Figure 10(b), it can be observed that during the two phases of accelerated geomagnetic anomaly growth, the pre-seismic b-value exhibits similar variations. Specifically, from day -80 to -60, the b-value first rises and then falls, peaking at day -73. From day -40 to -20, it reaches its maximum around day -30. An increase in b-value indicates enhanced release of stress through a higher frequency of seismic events. The temporal coincidence between the inflection points of the two anomaly acceleration phases and the peaks in b-value variation suggests that SW-NTF is capable of extracting geomagnetic anomalies related to seismic activity.

https://doi.org/10.5194/egusphere-2026-317
Preprint. Discussion started: 11 February 2026

Furthermore, we computed the spatial variation of b-values in the epicentral region at 30-day intervals. The region was first divided into 0.1°×0.1° grids. The b-value was then calculated for each grid within a spatial window of 5×5 grids centered on the target grid, requiring a minimum of 20 seismic events within each window. The resulting b-value was assigned to the corresponding grid cell to map the spatial variation (Chen et al., 2022).

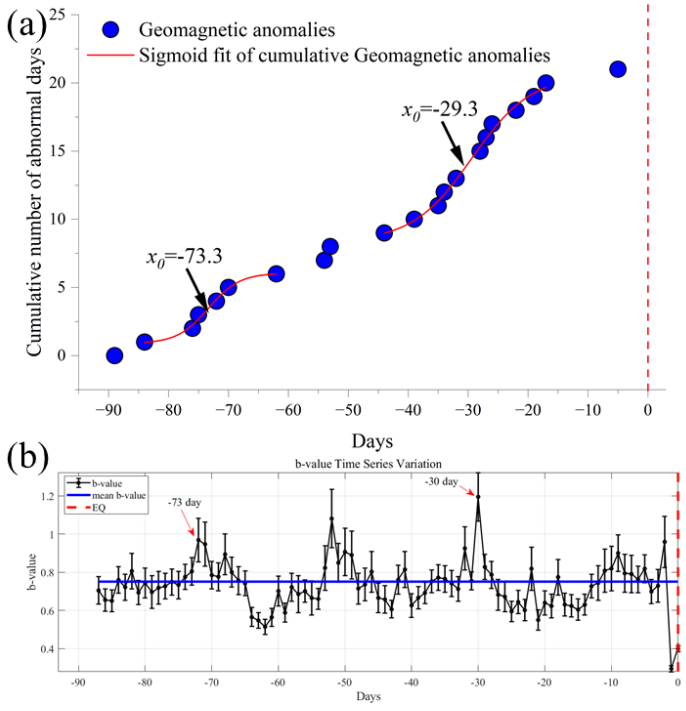

Figure 10: Comparison of temporal variations between geomagnetic anomalies and b-values. (a) Temporal cumulative results of geomagnetic anomalies, with the S-shaped curve representing the sigmoidal fit. (b) Temporal variation of b-values, where the blue line indicates the mean b-value. The red dashed line marks the mainshock.

Based on Figure 11, the following spatiotemporal evolution pattern can be observed. From day -90 to -60, the b-values southwest of the epicenter were approximately 1.0, indicating a stress release zone. During days -60 to -30, the b-values northeast of the epicenter exceeded 1.0, accompanied by frequent small earthquakes. Furthermore, from day -90 to -30, the strain release areas in the periphery of the epicenter expanded rapidly, became interconnected, and progressively engaged the entire fault zone (Ma and Guo, 2014). Consequently, the geomagnetic anomalies during this period were primarily contributed by stations distributed across this extensive region. From day -30 until the earthquake occurrence, stress release in the peripheral areas led to continuous stress accumulation in the epicentral region (Noda et al., 2013), with b-values dropping below 0.5. This signifies the locking of the epicentral area and marks the transition of the earthquake preparation into an irreversible stage. Accordingly, fewer anomalies were detected during this phase. Following the mainshock, the b-values began to recover as stress was released. This finding further demonstrates that the geomagnetic anomalies extracted in this study are associated with anomalous subsurface stress changes and may contain precursory information related to the Madoi earthquake

https://doi.org/10.5194/egusphere-2026-317
Preprint. Discussion started: 11 February 2026

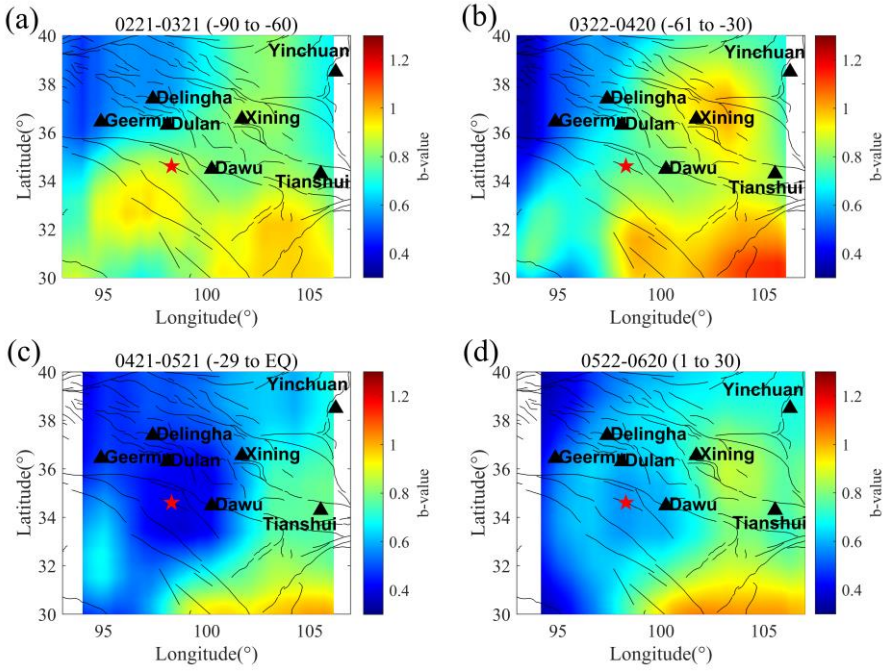

Figure 11: Spatial distribution of pre-seismic b-values. The four subpanels show the spatial variation of b-values over consecutive 30-day intervals, spanning from 90 days before to 30 days after the earthquake. The star denotes the epicenter, black triangles represent geomagnetic stations, and black lines indicate faults.

6 Conclusion

This study proposed a SW-NTF method to address the limitations of traditional NTF, which performs inadequately in decomposing geomagnetic station data due to the lack of prior information. The SW-NTF method was developed to extract fused pre-seismic magnetic anomalies from multiple stations. Using this improved approach, we investigated the spatiotemporal characteristics of geomagnetic anomalies preceding the 2021 Ms 7.4 Madoi earthquake. First, a third-order tensor was constructed daily from the daily 1 Hz Z-component geomagnetic data, recorded between local midnight (00:00–04:00 LT) at seven stations, covering a period from 90 days before to 30 days after the earthquake. The tensor was decomposed using the SW-NTF method to extract pre-seismic geomagnetic anomalies. The results were compared with those obtained from traditional NTF, and the spatiotemporal variation characteristics of the anomalies extracted by SW-NTF were analyzed. Subsequently, the potential influence of geomagnetic activity on the detected anomalies was examined. Furthermore, the variation characteristics of the pre-seismic geomagnetic anomalies were comparatively analyzed using magnetic field changes observed in rock loading experiments. In addition, to explore the relationship between geomagnetic anomalies and seismic activity, we compared the temporal cumulative characteristics of Benioff strain as well as the spatiotemporal distribution of pre-seismic b-values. The main findings are summarized as follows:

https://doi.org/10.5194/egusphere-2026-317
Preprint. Discussion started: 11 February 2026

(1) Compared to conventional NTF, SW-NTF introduces constraints based on station spatial locations into the optimization process. This enables it to more effectively separate signal components originating from the source region that exhibit clear spatial decay characteristics from the background field. As a result, SW-NTF may more directly correlate with the physical processes at the seismic source and improves the robustness of geomagnetic anomaly extraction.

(2) The pre-seismic geomagnetic anomalies extracted by the SW-NTF method exhibit two phases of S-shaped accelerated growth in the time domain, occurring from day -85 to -60 and from day -40 to -17, respectively. Spatially, the anomalies initially appeared at stations farther from the epicenter and gradually migrated toward and clustered at stations closer to the epicenter.

(3) The variation characteristics of pre-earthquake magnetic field anomalies correspond well with the magnetic field variation characteristics observed in rock loading experiments.

(4) The accelerated phases of the pre-seismic geomagnetic anomalies correspond well, in both time and space, with periods of frequent seismic activity during stress release stages. In addition, the quiescence of anomalies immediately before the mainshock appears to be associated with the locking of the seismogenic zone during the preparation process of the Madoi earthquake.

Code availability

The numerical process can be easily generated by everyone using the equations and indications of the text. If you have any problems, do not hesitate to write and ask the corresponding author or first author.

Data availability

Geomagnetic observation data is provided by the China Earthquake Networks Center, the National Earthquake Data Center. Due to licensing restrictions, the data are not publicly available. However, they can be obtained upon request to the China Earthquake Networks Center. All other data are open-source and can be accessed via the links provided in the paper.

Author contributions

B. Y.: Conceptualization, Data curation, Formal analysis, Investigation, Methodology Writing – original draft, Writing – review & editing. K. Z.: Funding acquisition, Project administration, Supervision. T. W.: Software, Writing – review & editing. D. Z.: Formal analysis, Investigation. W. C.: Visualization. Y. Z.: Writing – review & editing. P. W.: Writing – review & editing. X. L.: Writing – review & editing. Y. C.: Writing – review & editing.

https://doi.org/10.5194/egusphere-2026-317
Preprint. Discussion started: 11 February 2026

Competing interests

The authors declare no conflicts of interest.

Acknowledgements

The authors would like to acknowledge the China Earthquake Networks Center, the National Earthquake Data Center for providing the geomagnetic data (https://data.earthquake.cn/index.html) and earthquake catalog data (https://news.ceic.ac.cn/), the World Data Center for Geomagnetism for providing the Dst index and ap index data (https://wdc.kugi.kyoto-u.ac.jp/).

Financial support

This work was supported by the National Natural Science Foundation of China Key Program under Grant 42430113 and the National Natural Science Foundation of China under Grant 42374087.

Review statement

The review statement will be added by Copernicus Publications listing the handling editor as well as all contributing referees according to their status anonymous or identified.

References

BENIOFF, H.: SEISMIC EVIDENCE FOR THE FAULT ORIGIN OF OCEANIC DEEPS, GSA Bulletin, 60, 1837-1856, 1949.

Brace, W. F. and Byerlee, J. D.: Stick-Slip as a Mechanism for Earthquakes, Science, 153, 990-992, doi:10.1126/science.153.3739.990, 1966.

Chen, H., Han, P., and Hattori, K.: Ultralow-Frequency Geomagnetic Signal Estimation: An Interstation Transfer Function Method Based on Multivariate Wavelet Coherence, IEEE Transactions on Geoscience and Remote Sensing, 62, 1-11, 10.1109/TGRS.2024.3456433, 2024.

Chen, X., Li, Y., and Chen, L.: The characteristics of the b-value anomalies preceding the 2004 Mw9.0 Sumatra earthquake, Geomatics, Natural Hazards and Risk, 13, 390-399, 10.1080/19475705.2022.2029582, 2022.

Chi, E. C. and Kolda, T. G.: On Tensors, Sparsity, and Nonnegative Factorizations, SIAM Journal on Matrix Analysis and Applications, 33, 1272-1299, 10.1137/110859063, 2012.

De Santis, A., Cianchini, G., and Di Giovambattista, R.: Accelerating moment release revisited: Examples of application to Italian seismic sequences, Tectonophysics, 639, 82-98, 2015.

https://doi.org/10.5194/egusphere-2026-317
Preprint. Discussion started: 11 February 2026

De Santis, A., Balasis, G., Pavòn-Carrasco, F. J., Cianchini, G., and Mandea, M.: Potential earthquake precursory pattern from space: The 2015 Nepal event as seen by magnetic Swarm satellites, Earth and planetary science letters, 461, 119-126, 2017.

De Santis, A., Abbattista, C., Alfonsi, L., Amoruso, L., Campuzano, S. A., Carbone, M., Cesaroni, C., Cianchini, G., De Franceschi, G., De Santis, A., Di Giovambattista, R., Marchetti, D., Martino, L., Perrone, L., Piscini, A., Rainone, M. L., Soldani, M., Spogli, L., and Santoro, F.: Geosystemics View of Earthquakes, Entropy, 21, 412, 2019a.

De Santis, A., Marchetti, D., Spogli, L., Cianchini, G., Pavón-Carrasco, F. J., Franceschi, G. D., Di Giovambattista, R., Perrone, L., Qamili, E., Cesaroni, C., De Santis, A., Ippolito, A., Piscini, A., Campuzano, S. A., Sabbagh, D., Amoruso, L., Carbone, M., Santoro, F., Abbattista, C., and Drimaco, D.: Magnetic Field and Electron Density Data Analysis from Swarm Satellites Searching for Ionospheric Effects by Great Earthquakes: 12 Case Studies from 2014 to 2016, Atmosphere, 10, 371, 2019b.

Dobrovolsky, I. P., Zubkov, S. I., and Miachkin, V. I.: Estimation of the size of earthquake preparation zones, Pure & Applied Geophysics, 117, 1025-1044, 1979.

Fan, M., Zhu, K., Santis, A. D., Marchetti, D., Cianchini, G., Piscini, A., He, X., Wen, J., Wang, T., Zhang, Y., and Cheng, Y.: Analysis of Swarm Satellite Magnetic Field Data for the 2015 Mw 7.8 Nepal Earthquake Based on Nonnegative Tensor Decomposition, IEEE Transactions on Geoscience and Remote Sensing, 60, 1-19, 10.1109/TGRS.2022.3195726, 2022.

Fan, M., Zhu, K., Santis, A. D., Marchetti, D., Cianchini, G., Wang, T., Zhang, Y., Zhang, D., and Cheng, Y.: Exploration of the 2021 Mw 7.3 Maduo Earthquake by Fusing the Electron Density and Magnetic Field Data of Swarm Satellites, IEEE Transactions on Geoscience and Remote Sensing, 62, 1-24, 10.1109/TGRS.2024.3361875, 2024.

Feng, L., Zhu, W., Guan, Y., Fan, W., and Ji, Y.: A new method for extracting geomagnetic perturbation anomalies preceding the M7.4 Maduo earthquake, Physics of the Earth and Planetary Interiors, 359, 107305, https://doi.org/10.1016/j.pepi.2024.107305, 2025.

Fraser-Smith, A. C., Bernardi, A., McGill, P. R., Ladd, M. E., Helliwell, R. A., and Villard Jr., O. G.: Low-frequency magnetic field measurements near the epicenter of the Ms 7.1 Loma Prieta Earthquake, Geophysical Research Letters, 17, 1465-1468, https://doi.org/10.1029/GL017i009p01465, 1990.

Gentili, S., Peresan, A., Talebi, M., Zare, M., and Di Giovambattista, R.: A seismic quiescence before the 2017 Mw 7.3 Sarpol Zahab (Iran) earthquake: Detection and analysis by improved RTL method, Physics of the Earth and Planetary Interiors, 290, 10-19, https://doi.org/10.1016/j.pepi.2019.02.010, 2019.

Gokhberg, M. B., Morgounov, V. A., Yoshino, T., and Tomizawa, I.: Experimental measurement of electromagnetic emissions possibly related to earthquakes in Japan, J. Geophys. Res, 87, 7824-7828, 1982.

Gutenberg, B. and Richter, C. F.: Frequency of earthquakes in California, Bulletin of the Seismological Society of America, Vol.34, 185-188, 1944.

https://doi.org/10.5194/egusphere-2026-317
Preprint. Discussion started: 11 February 2026

Habarulema, J. B., Yizengaw, E., Katamzi-Joseph, Z. T., Moldwin, M. B., and Buchert, S.: Storm Time Global Observations of Large-Scale TIDs From Ground-Based and In Situ Satellite Measurements, Journal of Geophysical Research: Space Physics, 123, 711-724, https://doi.org/10.1002/2017JA024510, 2018.

Han, P., Hattori, K., Huang, Q., Hirano, T., Ishiguro, Y., Yoshino, C., and Febriani, F.: Evaluation of ULF electromagnetic phenomena associated with the 2000 Izu Islands earthquake swarm by wavelet transform analysis, Nat. Hazards Earth Syst. Sci., 11, 965-970, 10.5194/nhess-11-965-2011, 2011.

Han, P., Hattori, K., Hirokawa, M., Zhuang, J., Chen, C.-H., Febriani, F., Yamaguchi, H., Yoshino, C., Liu, J.-Y., and Yoshida, S.: Statistical analysis of ULF seismomagnetic phenomena at Kakioka, Japan, during 2001–2010, Journal of Geophysical Research: Space Physics, 119, 4998-5011, https://doi.org/10.1002/2014JA019789, 2014.

Hansen, S., Plantenga, T., and Kolda, T. G.: Newton-based optimization for Kullback–Leibler nonnegative tensor factorizations, Optimization Methods and Software, 30, 1002-1029, 10.1080/10556788.2015.1009977, 2015.

Hattori, K., Serita, A., Gotoh, K., Yoshino, C., Harada, M., Isezaki, N., and Hayakawa, M.: ULF geomagnetic anomaly associated with 2000 Izu Islands earthquake swarm, Japan, Physics and Chemistry of the Earth, Parts A/B/C, 29, 425-435, https://doi.org/10.1016/j.pce.2003.11.014, 2004.

Hattori, K.: ULF geomagnetic changes associated with large earthquakes, TERRESTRIAL ATMOSPHERIC AND OCEANIC SCIENCES, 15, 329-360, 10.3319/TAO.2004.15.3.329(EP), 2004.

Hattori, K., Han, P., and Huang, Q.: Global variation of ULF geomagnetic fields and detection of anomalous changes at a certain observatory using reference data, Electrical Engineering in Japan, 182, 9-18, https://doi.org/10.1002/eej.22299, 2013a.

Hattori, K., Han, P., Yoshino, C., Febriani, F., Yamaguchi, H., and Chen, C.-H.: Investigation of ULF Seismo-Magnetic Phenomena in Kanto, Japan During 2000–2010: Case Studies and Statistical Studies, Surveys in Geophysics, 34, 293-316, 10.1007/s10712-012-9215-x, 2013b.

Hayakawa, M.: Electromagnetic phenomena associated with earthquakes: A frontier in terrestrial electromagnetic noise environment, Recent Res. Devel. Geophysics, 6, 81-112, 2004.

Hayakawa, M., Kawate, R., Molchanov, O. A., and Yumoto, K.: Results of ultra-low-frequency magnetic field measurements during the Guam Earthquake of 8 August 1993, Geophysical Research Letters, 23, 241-244, https://doi.org/10.1029/95GL02863, 1996.

Hayakawa, M., Schekotov, A., Yamaguchi, H., and Hobara, Y.: Observation of Ultra-Low-Frequency Wave Effects in Possible Association with the Fukushima Earthquake on 21 November 2016, and Lithosphere-Atmosphere-Ionosphere Coupling, Atmosphere, 14, 1255, 2023.

He, X., Sun, X., Yin, S., Song, D., Qiu, L., Tong, Y., Wang, Q., and Li, J.: Experimental research on magnetic field variation in rock failure process and its significance for earthquake prediction, Chinese Journal of Geophysics, 66, 4609-4624, 2023.

Hitchcock, F. L.: Multiple Invariants and Generalized Rank of a P-Way Matrix or Tensor, Journal of Mathematics and Physics, 7, 39-79, https://doi.org/10.1002/sapm19287139, 1928.

https://doi.org/10.5194/egusphere-2026-317
Preprint. Discussion started: 11 February 2026

Huang, J., Jia, J., Yin, H., Li, Z., Li, J., Shen, X., and Zhima, Z.: Study of the Statistical Characteristics of Artificial Source Signals Based on the CSES, Frontiers in Earth Science, 10, 10.3389/feart.2022.883836, 2022.

Huang, Q.: Retrospective investigation of geophysical data possibly associated with the Ms8.0 Wenchuan earthquake in Sichuan, China, Journal of Asian Earth Sciences, 41, 421-427, https://doi.org/10.1016/j.jseaes.2010.05.014, 2011.

Jing, F., Zhang, L., and Singh, R. P.: Pronounced Changes in Thermal Signals Associated with the Madoi (China) M 7.3 Earthquake from Passive Microwave and Infrared Satellite Data, Remote Sensing, 14, 2539, 2022.

Kelley, M. C., Swartz, W. E., and Heki, K.: Apparent ionospheric total electron content variations prior to major earthquakes due to electric fields created by tectonic stresses, Journal of Geophysical Research: Space Physics, 122, 6689-6695, https://doi.org/10.1002/2016JA023601, 2017.

K., A.: Maximum likelihood estimate of b in the formula log N=a-bM and its confidence limits, Bull.Earthq.Res.Inst., Vol.43, 237-239, 1965.

Li, J., Chen, Y., Zhang, Z., Zhang, S., Yan, H., Chen, M., Zhan, W., Zhang, Y., Xu, W., Sun, R., Chen, G., and Wu, Y.: Early Viscoelastic Relaxation and After slip Inferred from the Post seismic Geodetic Observations Following the 2021 Mw7.4 Maduo Earthquake, Journal of Geophysical Research: Solid Earth, 130, e2024JB030466, https://doi.org/10.1029/2024JB030466, 2025.

Li, M. and Parrot, M.: "Real time analysis" of the ion density measured by the satellite DEMETER in relation with the seismic activity, Nat. Hazards Earth Syst. Sci., 12, 2957-2963, 10.5194/nhess-12-2957-2012, 2012.

Li, M. and Parrot, M.: Statistical analysis of an ionospheric parameter as a base for earthquake prediction, Journal of Geophysical Research Space Physics, 118, 3731-3739, 2013.

Li, H., Liu, T., Wu, X., and Chen, Q.: EEMD and optimized frequency band entropy for fault feature extraction of bearings, Journal of Vibration Engineering, 33, 414-423, 10.16385/j.cnki.issn.1004-4523.2020.02.022, 2020.

Liu, C., Zhu, L., and Ni, C.: Chatter detection in milling process based on VMD and energy entropy, Northeastern University, School of Mechanical Engineering and Automation, Shenyang, 110819, China, 12434, Vol.105, 169-182, 10.1016/j.ymssp.2017.11.046, 2018.

Liu, S., Cui, Y., Wei, L., Liu, W., and Ji, M.: Pre-earthquake MBT anomalies in the Central and Eastern Qinghai-Tibet Plateau and their association to earthquakes, Remote Sensing of Environment, 298, 113815, https://doi.org/10.1016/j.rse.2023.113815, 2023.

Loewe, C. A. and Prölss, G. W.: Classification and mean behavior of magnetic storms, Journal of Geophysical Research: Space Physics, 102, 14209-14213, https://doi.org/10.1029/96JA04020, 1997.

Marchetti, D. and Akhoondzadeh, M.: Analysis of Swarm satellites data showing seismo-ionospheric anomalies around the time of the strong Mexico (Mw = 8.2) earthquake of 08 September 2017, Advances in Space Research, 62, 614-623, https://doi.org/10.1016/j.asr.2018.04.043, 2018.

https://doi.org/10.5194/egusphere-2026-317
Preprint. Discussion started: 11 February 2026

Marchetti, D., De Santis, A., D'Arcangelo, S., Poggio, F., Jin, S., Piscini, A., and Campuzano, S. A.: Magnetic Field and Electron Density Anomalies from Swarm Satellites Preceding the Major Earthquakes of the 2016–2017 Amatrice-Norcia (Central Italy) Seismic Sequence, Pure and Applied Geophysics, 177, 305-319, 10.1007/s00024-019-02138-y, 2020a.

Marchetti, D., De Santis, A., Shen, X., Campuzano, S. A., Perrone, L., Piscini, A., Di Giovambattista, R., Jin, S., Ippolito, A., Cianchini, G., Cesaroni, C., Sabbagh, D., Spogli, L., Zhima, Z., and Huang, J.: Possible Lithosphere-Atmosphere-Ionosphere Coupling effects prior to the 2018 Mw = 7.5 Indonesia earthquake from seismic, atmospheric and ionospheric data, Journal of Asian Earth Sciences, 188, 104097, https://doi.org/10.1016/j.jseaes.2019.104097, 2020b.

Ma, J. and Guo, Y.: Accelerated synergism prior to fault instability: Evidence from laboratory experiments and an earthquake case, Seismology and Geology, 36, 547-561, 2014.

Marchetti, D., Zhu, K., Piscini, A., Ghamry, E., Shen, X., Yan, R., He, X., Wang, T., Chen, W., Wen, J., Zhang, Y., Cheng, Y., Fan, M., Zhang, D., Zhang, H., and Ventura, G.: Changes in the lithosphere, atmosphere, and ionosphere before and during the Mw=7.7 Jamaica 2020 earthquake, Remote Sensing of Environment, 307, 114146, https://doi.org/10.1016/j.rse.2024.114146, 2024.

Molchanov, O. A. and Hayakawa, M.: Generation of ULF electromagnetic emissions by microfracturing, Geophysical Research Letters, 22, 3091-3094, https://doi.org/10.1029/95GL00781, 1995.

Molchanov, O. A., Hayakawa, M., and Rafalsky, V. A.: Penetration characteristics of electromagnetic emissions from an underground seismic source into the atmosphere, ionosphere, and magnetosphere, Journal of Geophysical Research: Space Physics, 100, 1691-1712, https://doi.org/10.1029/94JA02524, 1995.

Moore, G. W.: Magnetic Disturbances preceding the 1964 Alaska Earthquake, Nature, 203, 508-509, 1964.

Noda, H., Nakatani, M., and Hori, T.: Large nucleation before large earthquakes is sometimes skipped due to cascade-up—Implications from a rate and state simulation of faults with hierarchical asperities, Journal of Geophysical Research: Solid Earth, 118, 2924-2952, https://doi.org/10.1002/jgrb.50211, 2013.

Ouyang, X. Y., Parrot, M., and Bortnik, J.: ULF Wave Activity Observed in the Nighttime Ionosphere Above and Some Hours Before Strong Earthquakes, Journal of Geophysical Research. Space Physics, 125, 2020.

Parrot, M., Achache, J., Berthelier, J. J., Blanc, E., and Villain, J. P.: High-frequency seismo-electromagnetic effect, Physics of The Earth and Planetary Interiors, 77, 65-83, 1993.

Pulinets, S.: Lithosphere–atmosphere–ionosphere coupling (laic) model, Electromagnetic Phenomena Associated with Earthquakes2004.

Rehman, N. and Mandic, D. P.: Multivariate empirical mode decomposition, Department of Electrical and Electronic Engineering, Imperial College London, London SW7 2AZ, UK, Vol.466, 1291-1302, 10.1098/rspa.2009.0502, 2010.

Ruzhin, Y. Y., Larkina, V., and Depueva, A. K.: Earthquake precursors in magnetically conjugated ionosphere regions, Advances in Space Research, 21, 525-528, 1998.

https://doi.org/10.5194/egusphere-2026-317
Preprint. Discussion started: 11 February 2026

Schekotov, A. Y., Molchanov, O. A., Hayakawa, M., Fedorov, E. N., Chebrov, V. N., Sinitsin, V. I., Gordeev, E. E., Belyaev, G. G., and Yagova, N. V.: ULF/ELF magnetic field variations from atmosphere induced by seismicity, Radio Science, 42, https://doi.org/10.1029/2005RS003441, 2007.

Scholz, C. H.: The frequency-magnitude relation of microfracturing in rock and its relation to earthquakes, Bulletin of the Seismological Society of America, 58, 399-415, 10.1785/bssa0580010399, 1968.

Scholz, C. H.: Mechanisms of seismic quiescences, pure and applied geophysics, 126, 701-718, 10.1007/BF00879016, 1988.

Scholz, C. H., Sykes, L. R., and Aggarwal, Y. P.: Earthquake Prediction: A Physical Basis, Science, 181, 803-810, 1973.

Schorlemmer, D., Wiemer, S., and Wyss, M.: Variations in earthquake-size distribution across different stress regimes, Nature, 437, 539-542, 10.1038/nature04094, 2005.

Shashua, A. and Levin, A.: Linear image coding for regression and classification using the tensor-rank principle, Proceedings of the 2001 IEEE Computer Society Conference on Computer Vision and Pattern Recognition. CVPR 2001, 8-14 Dec. 2001, I-I, 10.1109/CVPR.2001.990454,

Utada, H., Shimizu, H., Ogawa, T., Maeda, T., Furumura, T., Yamamoto, T., Yamazaki, N., Yoshitake, Y., and Nagamachi, S.: Geomagnetic field changes in response to the 2011 off the Pacific Coast of Tohoku Earthquake and Tsunami, Earth and Planetary Science Letters, 311, 11-27, https://doi.org/10.1016/j.epsl.2011.09.036, 2011.

Venegas-Aravena, P., Cordaro, E. G., and Laroze, D.: A review and upgrade of the lithospheric dynamics in context of the seismo-electromagnetic theory, Nat. Hazards Earth Syst. Sci., 19, 1639-1651, 10.5194/nhess-19-1639-2019, 2019.

Wiemer, S. and Wyss, M.: Minimum Magnitude of Completeness in Earthquake Catalogs: Examples from Alaska, the Western United States, and Japan, Bulletin of the Seismological Society of America, 90, 859-869, 10.1785/0119990114, 2000.

Wyss, M.: Evaluation of Proposed Earthquake Precursors, Eos, Transactions American Geophysical Union, 72, 411-411, https://doi.org/10.1029/90EO10300, 1991.

Wyss, M.: Second round of evaluations of proposed earthquake precursors, pure and applied geophysics, 149, 3-16, 10.1007/BF00945158, 1997.

Wyss, M., Console, R., and Murru, M.: Seismicity rate change before the Irpinia (M = 6.9) 1980 earthquake, Bulletin of the Seismological Society of America, 87, 318-326, 10.1785/BSSA0870020318, 1997.

Xie, T., Chen, B., Wu, L., Dai, W., Kuang, C., and Miao, Z.: Detecting Seismo-Ionospheric Anomalies Possibly Associated With the 2019 Ridgecrest (California) Earthquakes by GNSS, CSES, and Swarm Observations, Journal of Geophysical Research: Space Physics, 126, e2020JA028761, https://doi.org/10.1029/2020JA028761, 2021.

Xue, J., Huang, Q., Wu, S., and Zhao, L.: Detection of ULF Geomagnetic Anomalies Prior to the Tohoku-Oki Earthquake by the Multireference Station Method, IEEE Transactions on Geoscience and Remote Sensing, 62, 1-9, 10.1109/TGRS.2024.3382472, 2024.

https://doi.org/10.5194/egusphere-2026-317
Preprint. Discussion started: 11 February 2026

Xue, L., Qin, S., Sun, Q., Wang, Y., Lee, L. M., and Li, W.: A Study on Crack Damage Stress Thresholds of Different Rock Types Based on Uniaxial Compression Tests, Rock Mechanics and Rock Engineering, 47, 1183-1195, 10.1007/s00603-013-0479-3, 2014.

Yang, B.-Y., Li, Z., Huang, J.-P., Yang, X.-M., Yin, H.-C., Li, Z.-Y., Lu, H.-X., Li, W.-J., Shen, X.-H., Zeren, Z., Tan, Q., and Zhou, N.: EMD based statistical analysis of nighttime pre-earthquake ULF electric field disturbances observed by CSES, Frontiers in Astronomy and Space Sciences, 9, 10.3389/fspas.2022.1077592, 2023.

Yang, B., Zhu, K., Wang, T., Zhang, D., Chen, W., Zhang, Y., Wang, P., and Cheng, Y.: Spatiotemporal Evolution Characteristics of Outgoing Longwave Radiation (OLR) Anomalies Before the 2021 Ms7.4 Madoi Earthquake, IEEE Journal of Selected Topics in Applied Earth Observations and Remote Sensing, 18, 25721-25734, 10.1109/JSTARS.2025.3614629, 2025.

Yao, Y., Liu, L., Kong, J., and Zhai, C.: Analysis of the global ionospheric disturbances of the March 2015 great storm, Journal of Geophysical Research: Space Physics, 121, 12,157-112,170, https://doi.org/10.1002/2016JA023352, 2016.

Yu, Z., Hattori, K., Zhu, K., Chi, C., Fan, M., and He, X.: Detecting Earthquake-Related Anomalies of a Borehole Strain Network Based on Multi-Channel Singular Spectrum Analysis, Entropy, 22, 1086, 2020.

Zhang, X., Qian, J., Ouyang, X., Shen, X., Cai, J. a., and Zhao, S.: Ionospheric electromagnetic perturbations observed on DEMETER satellite before Chile M7.9 earthquake, Earthquake Science, 22, 251-255, 10.1007/s11589-009-0251-7, 2009.

Zhang, Y., Li, M., Huang, Q., Shao, Z., Liu, J., Zhang, X., Ma, W., and Parrot, M.: Statistical Correlation Between DEMETER Satellite Electronic Perturbations and Global Earthquakes with M ≥ 4.8, IEEE Transactions on Geoscience and Remote Sensing, 61, 1-18, 10.1109/TGRS.2023.3265931, 2023.

Zhima, Z., Xuhui, S., Xuemin, Z., Jinbin, C., Jianping, H., Xinyan, O., Jing, L., and Lu, B.: Possible Ionospheric Electromagnetic Perturbations Induced by the Ms7.1 Yushu Earthquake, Earth, Moon, and Planets, 108, 2012.

Zhu, K., Fan, M., He, X., Marchetti, D., Li, K., Yu, Z., Chi, C., Sun, H., and Cheng, Y.: Analysis of Swarm Satellite Magnetic Field Data Before the 2016 Ecuador (Mw = 7.8) Earthquake Based on Non-negative Matrix Factorization, Frontiers in Earth Science, 9, 10.3389/feart.2021.621976, 2021.

Zlotnicki, J., Le Mouël, J. L., Kanwar, R., Yvetot, P., Vargemezis, G., Menny, P., and Fauquet, F.: Ground-based electromagnetic studies combined with remote sensing based on Demeter mission: A way to monitor active faults and volcanoes, Planetary and Space Science, 54, 541-557, https://doi.org/10.1016/j.pss.2005.10.022, 2006.